



**HAL**  
open science

## Multi-instrument study of the upstream region near Mars' The Phobos 2 observations

E. Dubinin, K. Sauer, M. Delva, R. Grard, S. Livi, R. Lundin, A. Skalsky, K.  
Schwingenschuh, K. Szego, Jean-Gabriel Trotignon

### ► To cite this version:

E. Dubinin, K. Sauer, M. Delva, R. Grard, S. Livi, et al.. Multi-instrument study of the upstream region near Mars' The Phobos 2 observations. *Journal of Geophysical Research*, 2000, 105 (A4), pp.7557-7571. 10.1029/1999JA900400 . insu-03007465

**HAL Id: insu-03007465**

**<https://insu.hal.science/insu-03007465>**

Submitted on 16 Nov 2020

**HAL** is a multi-disciplinary open access archive for the deposit and dissemination of scientific research documents, whether they are published or not. The documents may come from teaching and research institutions in France or abroad, or from public or private research centers.

L'archive ouverte pluridisciplinaire **HAL**, est destinée au dépôt et à la diffusion de documents scientifiques de niveau recherche, publiés ou non, émanant des établissements d'enseignement et de recherche français ou étrangers, des laboratoires publics ou privés.

## Multi-instrument study of the upstream region near Mars: The Phobos 2 observations

E. Dubinin,<sup>1</sup> K. Sauer,<sup>1</sup> M. Delva,<sup>2</sup> R. Grard,<sup>3</sup> S. Livi,<sup>1</sup> R. Lundin,<sup>4</sup>  
A. Skalsky,<sup>5</sup> K. Schwingenschuh,<sup>2</sup> K. Szego,<sup>6</sup> and J.-G. Trotignon<sup>7</sup>

**Abstract.** Multi-instrument data analysis of the observations made by the Phobos 2 spacecraft in the upstream Martian environment shows that the solar wind deceleration observed in elliptical and circular orbits and previously referred to as mass loading by planetary exosphere occurs mainly in the foreshock region. Variations of the bulk speed are accompanied by strong magnetic field perturbations. The flow and field perturbations are well correlated, indicating their Alfvén wave origin. The data suggest that the observed disturbances are caused by large-amplitude Alfvén waves propagating in the solar wind as well as by waves generated locally at the foreshock. It is shown that the foreshock boundary is not just a topological boundary separating the regions either magnetically connected or disconnected with the bow shock. The transition across the tangent line is often accompanied with a sharp rotation of the magnetic field, decrease of the magnetic field value, and increase of the proton number density and temperature. Although variations of the solar wind speed at  $R \geq 6000$  km are mainly controlled by Alfvén waves, at closer distances to the planet, where the solar wind slows down at 150-200 km s<sup>-1</sup>, perturbations of the field and velocity do not follow the relation common for Alfvén waves. This strong deceleration can be attributed to mass loading on oxygen atmosphere.

### 1. Introduction

The measurements made by the Phobos 2 spacecraft provided us with a lot of information concerning the solar wind/Mars interaction, although many questions remain open. One of such critical questions is a problem of mass loading near Mars. Pedersen *et al.* [1991], Verigin *et al.* [1991], and Barabash *et al.* [1991] have reported that interaction of the solar wind with Mars starts far upstream from the bow shock as a consequence of extended neutral corona. This feature provides a certain resemblance of Mars with comets. Prob-

ably, the most abundant neutral component at large distances is molecular and atomic hydrogen, which can reach very high altitudes as the consequence of the weak gravitational attraction of Mars. Electron dissociative recombination of O<sub>2</sub><sup>+</sup> might be a source of hot atomic oxygen atoms which can also escape far away [Nagy and Cravens, 1988; Ip, 1988; Ip, 1990; Lammer and Bauer, 1991; Kim *et al.*, 1998]. The Phobos 2 observations were made during solar maximum activity when the density of hydrogen constituents (H and H<sub>2</sub>) is expected to decrease, although the upper atmosphere and the ionosphere dominated by molecular oxygen ions O<sub>2</sub><sup>+</sup> should extend to higher altitudes. Although the existence of hot oxygen corona near Mars was not confirmed, it is expected that the corona is denser than near Venus, where it was observed by the Pioneer Venus Orbiter (PVO) spacecraft [Kim *et al.*, 1998]. A hot hydrogen population produced by the photodissociation of molecular hydrogen has also been recorded at Venus, but not at Mars. It was believed that hot hydrogen and oxygen coronas, if they exist, are rare not affecting the solar wind to any major degree [Nagy *et al.*, 1990]. If coronas are not very rare the ionization and subsequent pickup of the exosphere matter by the solar wind may provide a mass loading effect similar to one near comets [Neugebauer, 1990]. The observations of wave emissions at the proton gyrofrequency is an indirect sign of pickup ions, protons or oxygen ions [Russell *et al.*, 1990; Sauer *et al.*, 1999]. Barabash *et al.* [1991] attributed the sec-

<sup>1</sup>Max-Planck Institut für Aeronomie, Katlenburg-Lindau, Germany.

<sup>2</sup>Institut für Weltraumforschung, Österreichischen Akademie der Wissenschaften, Graz, Austria.

<sup>3</sup>Space Sciences Department, European Space Agency, Noordwijk, The Netherlands.

<sup>4</sup>Swedish Institute of Space Physics, Kiruna, Sweden.

<sup>5</sup>Space Research Institute, Moscow, Russia.

<sup>6</sup>KFKI Research Institute for Particle and Nuclear Physics, Hungarian Academy of Sciences, Budapest, Hungary.

<sup>7</sup>Laboratoire de Physique et de Chimie de l'Environnement, Orleans, France.

Copyright 2000 by the American Geophysical Union.

Paper number 1999JA900400.  
0148-0227/00/1999JA900400\$09.00

ondary peaks in the spectrograms of proton fluxes upstream from the bow shock to picked-up protons. Researchers estimated the number density of the planetary protons of  $\sim 0.01n_{sw}$ . Small intensities of oxygen ions ( $\leq 10^{-4} \text{ cm}^{-3}$ ) were also recorded [Kirsch *et al.*, 1991]. On the contrary, Pedersen *et al.* [1991] reported about a much higher growth rate of the plasma density with decreasing distance from the planet by measuring a gradual decrease of the spacecraft floating potential. Under some assumptions, researchers derived the electron number density along the orbit and found that a distinct increase of the plasma number density starts far upstream from the Martian bow shock. The electron number density increased by  $1 - 2 \text{ cm}^{-3}$  between the undisturbed solar wind and the outer limit of the shock foot. However, on two of five elliptical orbits a gradual decrease of the floating potential was not observed that provided problems in the interpretation in terms of "standard" MHD mass loading. Verigin *et al.* [1991] have observed the essential solar wind deceleration upstream of the bow shock and attributed these measurements to mass loading on the hot oxygen corona. Assuming an instantaneous assimilation of planetary ions to the solar wind, Verigin *et al.* [1991] suggested that the oxygen corona near Mars is 5 times denser than predicted by the model of Ip [1988]. Since the model [Ip, 1988] overestimated the number density in the hot oxygen corona for solar maximum conditions at a factor of 2 - 3 [see Ip, 1990], the value given by [Verigin *et al.*, 1991] far exceeds even the "extreme" number density. Kotova *et al.* [1997] made a statistical study of the solar wind deceleration near Mars. They selected inbound and outbound passes of Phobos 2 on the circular orbits at  $2.8R_M$ , making the assumption that for the averaged interplanetary magnetic field (IMF) configuration quasi-perpendicular shocks are mostly in inbound legs while quasi-parallel shocks are met in outbound legs. They found that the solar wind deceleration turned to be approximately dawn-dusk symmetric and suggested that it is caused by mass loading on a hot oxygen corona with number density of neutrals at  $\sim 3$  times higher than the values from the extreme model. Recent reexamination of the population of hot oxygen atoms at Mars for the high solar cycle values made by [Kim *et al.*, 1998] gives the hot oxygen density nearly an order of magnitude less than estimates by [Kotova *et al.*, 1997]. Ip [1990] argued that mass loading by oxygen ions was unlikely to be the cause of the solar wind deceleration because reported deceleration requires a much more massive oxygen corona than can be expected from the models. Ip [1992] suggested that the reflection at the bow shock of  $\text{H}^+$  ions originating from the extended atomic hydrogen atmosphere of Mars could cause the slowdown of the solar wind. The importance of pickup ion reflection is motivated by the significant fraction of pickup protons with small normal velocity components at the bow shock that prevent their overcoming the electrostatic barrier. A fraction

of reflected ions is mass-dependent  $\sim (m_p/m_{\text{pick}})^{1/2}$ , where  $m_p$  and  $m_{\text{pick}}$  are masses of protons and pickup ions, respectively [Zank *et al.*, 1996], and heavy pickup ion species ( $\text{He}^+$ ,  $\text{O}^+$ ) less effectively participate in this process. Analyzing the measurements made by the sensor looking in the antisunward direction with field of view  $72^\circ \times 5^\circ$ , Barabash and Lundin [1993] have estimated the density of reflected protons in front of the bow shock foot as  $\leq 5\% n_{sw}$ . Dubinin *et al.* [1994a] have simulated the dynamics of pickup protons and have shown that the reflected pickup protons essentially contribute to the background of planetary ions upstream of the bow shock. A redistribution of pickup protons due to their reflection at the bow shock (ions occupy mainly the foreshock region) qualitatively explained the difference in the electron number density derived from the floating potential measurements on different elliptical orbits. An enhancement of mass loading was observed when the spacecraft encountered a bunch of reflected photoions [Dubinin and Lundin, 1995].

On the other hand, it is known that the deceleration of the solar wind is also effective in the Earth's foreshock [Bonifazi *et al.*, 1980; Zhang *et al.*, 1995, 1997], and a problem to distinguish between typical foreshock features and mass loading effects appears in the Mars case. Observations made on the Phobos 2 spacecraft suggested a large developed foreshock, which is similar to that known from wave and plasma observations at Earth. The electron foreshock adjacent to the tangent line was identified from the observations of bursts of electron plasma waves accompanied by the fluxes of backstreaming electrons [Skalsky *et al.*, 1992, 1993]. At farther distances from the tangent line, a broadband electric field noise and ULF waves characteristic of the ion foreshock were observed [Grard *et al.*, 1991; Delva and Dubinin, 1998]. Barabash and Lundin [1993] found typical foreshock signatures such as gyrating reflected ions and field-aligned beams. Otherwise, Brecht [1997a,b] argued that because of small size of Mars, effects of the ion gyroradii can strongly influence not only the bow shock structure but the Martian atmosphere too.

As will be shown in this paper, the position of the spacecraft with respect to the foreshock strongly varies along the orbit (the spacecraft often makes short tours into the undisturbed solar wind and back to the foreshock) that provides significant variations in the solar wind velocity. Therefore identification of foreshock or mass loading signatures becomes ambiguous without reliable awareness of the foreshock geometry and the spacecraft position. The solar wind/foreshock interface is also characterized by significant perturbations. The onset of electric field emissions ( $\sim 100 \text{ Hz}$ ) at the leading edge of the electron foreshock was reported by [Skalsky *et al.*, 1998] as the unique feature of the Martian upstream wave environment. Noticeable bending of the magnetic field lines near the tangent line was noticed by [Dubinin *et al.*, 1998a]. Bipolar variations of

the magnetic field were centered at the plane, which is normal to the tangent surface and intersects the bow shock at tangent points.

Thus a rather complex picture emerges from the data provided by different plasma instruments on board the Phobos 2 spacecraft. The purpose of the paper is to get a more detailed and less controversial picture of upstream region near Mars using the database of different plasma instruments. In this paper, we show that the disturbed structure of the upstream region is driven by time-varying perturbations in the solar wind (propagating large-amplitude Alfvén waves) as well as by local processes within foreshock. The relevance of these results to the problem of mass loading in the upstream region of Mars is also discussed.

## 2. Instrumentation

Parameters of the solar wind plasma were measured by the ion spectrometer (TAUS), which was well adapted to solar wind monitoring. The instrument has field of view  $40^\circ \times 40^\circ$  along the sunward direction, divided at  $8 \times 8$  sectors [Rosenbauer *et al.*, 1990]. The energy range was 30 eV to 6 keV, but most of the data were obtained in range 150 eV to 6 keV. The location of the spacecraft with respect to the foreshock is determined from the magnetic field measurements and the model of the bow shock. The magnetic fields near Mars (MAGMA) experiment was the three-axial fluxgate magnetometer with time sampling 1.5 or 45 s [Riedler *et al.*, 1989]. The three-dimensional geometry of the foreshock could be evaluated from the magnetic field data because the motion of the backstreaming particles is guided by the magnetic field lines, and therefore magnetic connection to the bow shock is bounded by the magnetic field line tangent to the bow shock. We use the coordinate system with the  $X$  axis positive to the Sun (antiparallel to  $\mathbf{V}_{sw}$ ) and the  $(\mathbf{V}_{sw}\mathbf{B})$  plane as the  $(XY^*)$  reference plane, where the  $Y^*$  axis is taken positive in the direction of the cross-flow component of  $\mathbf{B}$  (and thus always  $B_{y^*} \geq 0$ ), and the  $Z^*$  axis perpendicular to  $(X, Y^*)$  completes the system. The bow shock was approximated by a half ellipsoid of revolution around the  $X$  axis, in the  $(X, Y^*)$  magnetic equatorial plane [Trotignon *et al.*, 1991; Delva and Dubinin, 1998], and the angle  $\alpha$  between the tangent line and the direction to the spacecraft from the tangent point was evaluated. Positive values of angle  $\alpha$  ( $0^\circ - 180^\circ$ ) correspond to the location of the spacecraft in the foreshock. Negative values of  $\alpha$  ( $-180^\circ - 0^\circ$ ) give the position in the solar wind (Figure 1).

The foreshock geometry may be also traced by an appearance of electron plasma oscillations measured by the wave instrument. The Plasma Wave System (PWS) on board the Phobos 2 spacecraft consisted of bank of filters in frequency range 0.2 Hz to 150 kHz [Grard *et al.*, 1989a]. In this paper we use only the data collected in the high-frequency channels (6-38 kHz), which were

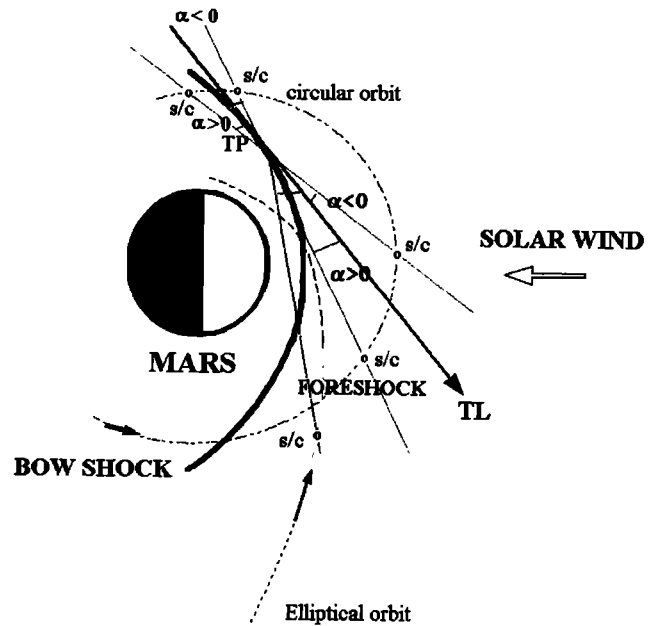


**Figure 1.** Projections of the elliptical and circular orbits of Phobos 2 onto the  $XY$  Mars solar orbital (MSO) plane and the average IMF configuration. The angle  $\alpha$  determines the position of the spacecraft with respect to the tangent line. Positive/negative values of the angle  $\alpha$  correspond to the foreshock region and the undisturbed solar wind, respectively.

attributed to the electron plasma waves [Grard *et al.*, 1989b; Skalsky *et al.*, 1992; Trotignon *et al.*, 1992], and low frequency emissions at frequencies between 0.2 and 10 Hz. The electron plasma oscillations are generated by the electrons, which are reflected at the bow shock and streaming sunward along the interplanetary magnetic field connected to the shock. Thus the observation of electron plasma oscillations is a very sensitive indicator of the magnetic field geometry. They appear to be close to the tangent line and mark the upstream edge of the electron foreshock. ULF waves are generated when ions backstreaming from the bow shock or ions of planetary origin interact with oncoming solar wind.

The foreshock geometry is also determined from inspection of antisunward/sunward anisotropy of electron heat fluxes. The Automatic Space Plasma Experiment with a Rotating Analyzer (ASPERA) contained the electron spectrometer (1 eV to 50 keV) and fluid electron parameters were calculated on board [Lundin *et al.*, 1989]. However, in contrast to ions, calculation of the moments of electron distribution function is very sensitive to the spacecraft potential and to photoelectrons. The standard procedure used to account for these effects is to adjust the electron number density  $n_e$  and electron bulk velocity  $V_e$  in such way that they were in reasonable agreement with the proton number density and proton bulk velocity, respectively, assuming quasi-neutrality. The on board calculations usually do not

take these factors into account. To avoid a contribution from photoelectrons the external grid of the electron spectrometer was biased at  $-12$  V and a part of a core of the distribution near  $V_e$  was missed. Then, the second moment of the electron distribution function  $M$ , which is related to the measured differential directional flux  $j$  ( $M = \int j(E, \theta, \varphi) dE H(\theta, \varphi)$ ), where  $\theta, \varphi$ , and  $H$  are the elevation angle determined by the sensors, the azimuth (scan) angle, and trigonometric vector, respectively), primarily gives information about asymmetry in wings of the electron distribution functions. An asymmetry could be supplied by solar wind halo electrons carrying the heat flux from the solar corona. *Dubinina et al.* [1994b] have applied the measurements of electrons in wings as tracers of the Martian tail topology because streaming electrons replicate field line kinks associated with draping of the IMF around Mars. This approach [*Dubinina et al.*, 1994b] provides us with a very sensitive tool for the study of the magnetosphere topology. Planetary bow shocks give rise to another source of electron heat flux propagating in the opposite, sunward direction. Therefore a sign of  $M_x$  is determined by a relative contribution of both sources. Negative values of  $M_x$  correspond to electron heat flux from the solar corona carried by electrons along the IMF. In the electron foreshock, heat fluxes in the sunward direction, associated with electrons accelerated and reflected at the bow shock, can dominate the anisotropy in the wings and change its sign.

The measurements of the difference potential between a conductive surface of the spacecraft at floating potential and electric field probe, negatively biased in relation to the spacecraft, were used to determine electron number density [*Pedersen et al.*, 1991]. The probe was biased with a current limited to 50 nA by a high impedance current source that drives the probe potential more negative in relation to the positive spacecraft by an amount  $\Delta V$ . This quantity, measured as a potential difference between a floating spacecraft and a biased probe, is inversely proportional to the electron number density. Uncertainty of this technique is related to the absence of information about the electron energy also affecting the floating potential. Nevertheless, the  $\Delta V - n_e$  relation is very sensitive to variations in  $n_e$  and can be used as indicator of mass loading features [*Dubinina et al.*, 1994a].

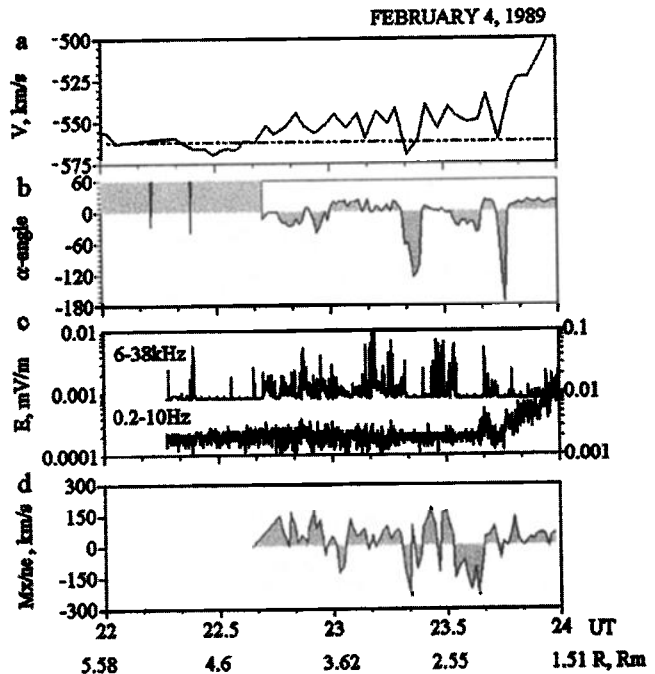
There were two main types of Phobos 2 orbits around Mars (Figure 1). During the first stage of the mission, the orbit spacecraft was elliptical with a periapsis altitude of 850 km and a period of 76.5 hours. Most observations were done when the spacecraft was settled on the circular orbit ( $R \sim 2.8R_M$ ). In some orbits the spacecraft was three axis stabilized, while in other orbits, Phobos 2 was in a spinning mode with the axis of rotation intended to be pointing to the Sun. However, the axis of rotation was really deviating from this direction, and the additional despun processing of the magnetic field data was done [*Delva et al.*, 1993]. Al-

though the bulk velocity of the solar wind could be reliably evaluated even when the spacecraft was spinning, fine details of variations of plasma number density was acquired only from stabilized orbits or from the measurements of the floating potential.

### 3. Observations

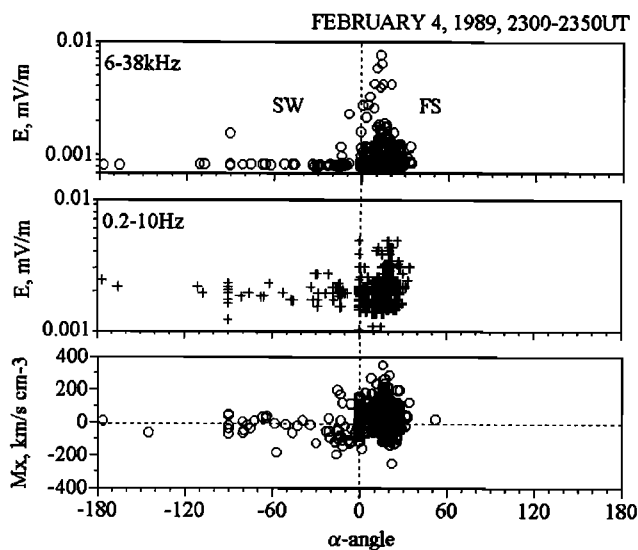
#### 3.1. Elliptical Orbits

Figure 2 shows the measurements made by the different experiments along the elliptical orbit on February 4-5, 1989. Figure 2a gives variations of the proton bulk velocity. Despinning magnetic field data were used to determine the position of the spacecraft relative to the foreshock. Figure 2b presents the angle  $\alpha$  between the magnetic field line tangent to the bow shock and the direction to the spacecraft from tangent point. Gaps indicate when the magnetic field does not intersect the shock. Figure 2c shows the amplitude of high-frequency (6-38 kHz) and low-frequency (0.2-10 Hz) waves. Figure 2d contains the second moment of the electron distribution function  $M_x$  divided by the electron number density. Entry of the spacecraft into the foreshock was at 2240 UT. Subsequent variations of sign of the angle  $\alpha$  indicate that the spacecraft makes often excursions to the solar wind. The spikes of the electron plasma emissions (6-38 kHz) clearly mark the crossings of the electron



**Figure 2.** (a) The solar wind velocity, (b) the angle  $\alpha$ , (c) amplitudes of electron plasma oscillations (scale is on the left side) and low-frequency waves (scale is on the right side), and (d) the second moment of the electron distribution function divided by the density ( $|V_e| \geq 1500$  km s $^{-1}$ ) during the elliptical orbit on February 4-5, 1989. Planetocentric distance  $R$  is in Mars radii ( $R_M = 3388$  km).

foreshock. The foreshock geometry and position of the spacecraft with respect to the foreshock were also determined from the inspection of antisunward/sunward anisotropy of fluxes of suprathermal electrons. Negative values of  $M_x$  in the upstream solar wind point out that the prevalent electron heat flux from the solar corona is mostly carried by electrons along the interplanetary magnetic field. When the spacecraft arrives at the electron foreshock, heat fluxes in the sunward direction associated with electrons accelerated and reflected at the bow shock begin to dominate and change sign of the anisotropy ( $M_x > 0$ ). It is seen that the sunward fluxes of suprathermal electrons mostly dominate over fluxes related to the solar wind halo electrons after 2240 UT. At 2320-2325 UT and 2332-2340 UT, the spacecraft was outside the foreshock in the solar wind ( $\alpha < 0$ ). Clear dropouts of plasma emissions and signatures of halo electrons ( $M_x < 0$ ) are observed. It is also seen that identification of the foreshock/upstream region based on the model bow shock and the local magnetic field measurements is not always perfect. For example, according to the model calculations, the spacecraft was in the solar wind at 2245-2252 UT, although the observations of electron plasma waves and fluxes of backstreaming electrons indicate a magnetic connection with the bow shock. Although, in most cases the model predictions are in a reasonable agreement with the observations, only negative values of the angle  $\alpha$  associated with disappearance of the electron plasma emissions and, to a lesser extent, change of the anisotropy of the halo electrons are discriminators of back excursion to the solar wind. In Figure 3 the observations of electron plasma waves and backstreaming electrons are plotted versus the angle  $\alpha$ . A general trend, showing that electron plasma oscillations and sunward fluxes of



**Figure 3.** Amplitude of electron plasma and ULF waves, and the flux of the suprathermal electrons versus the angle  $\alpha$  (February 4, 1989).

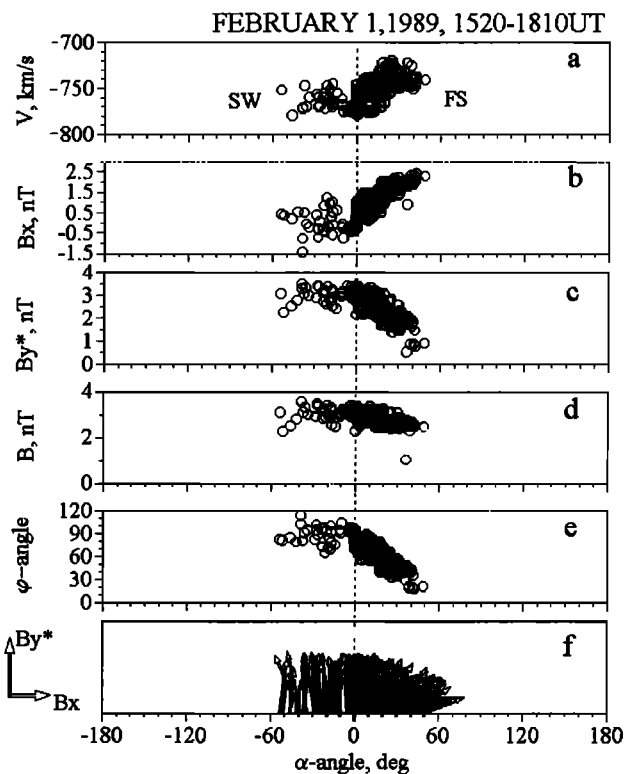


**Figure 4.** Dependence of the solar wind velocity and the magnetic field on the angle  $\alpha$  in the upstream region for the orbit on February 1, 1989. (a) The solar wind velocity  $V$ , (b) the  $B_x$  and (c)  $B_{y^*}$  components of the magnetic field, (d) the magnetic field magnitude  $B$ , (e) the cone angle  $\varphi$ , and (f) vectors of the magnetic field in the  $XY^*$  plane are given.

suprathermal electrons ( $M_x > 0$ ) appear close to the tangent line crossing ( $\alpha = 0$ ), justifies the use of the model position of the bow shock. In accordance with expectations, low-frequency waves prevail at larger distances from the tangent line in the ion foreshock where the density of high-intensity points is greater.

A remarkable feature of Figure 2 is that the solar wind deceleration starts close to the foreshock boundary (2240 UT). While the spacecraft made excursions into the solar wind, excepting the interval between 2332 and 2340 UT, the proton velocity was recovered to its "nominal" upstream value of the velocity computed from an upstream time interval in the solar wind (horizontal dashed line). After 2345 UT, when the spacecraft approached the bow shock at the distance less than  $\sim 1700$  km, deceleration of the solar wind becomes evident. Strong increase of the ULF turbulence (0.2-10 Hz) marks this region well. The bow shock was crossed at 0003 UT on February 5.

In Figure 4 the solar wind velocity and the magnetic field are plotted versus the angle  $\alpha$  for the orbit on February 1, 1989. The solar wind velocity  $V$  (Figure 4a), the  $B_x$  and  $B_{y^*}$  components of the magnetic field (Figures 4b and 4c), the magnetic field magnitude

$B$ , (Figure 4d) the cone angle  $\varphi$  (the angle between  $X$  axis and the magnetic field vector  $\mathbf{B}$ ) (Figure 4e). Figure 4f presents the projection of the magnetic field onto the  $XY^*$  plane versus the angle  $\alpha$ . The velocity decreases with increase of the angle  $\alpha$  in the foreshock region ( $\alpha > 0$ ) without visible speed variations in the undisturbed solar wind ( $\alpha < 0$ ). A gradual rotation of the magnetic field vector is also clearly observed. This rotation is not surprising because the angle  $\alpha$  is determined from the magnetic field measurements. If, for example, the magnetic field vector turns toward the  $X$  axis, an observer in the foreshock occurs farther from the tangent line, at larger  $\alpha$  angles. The interesting point is, however, that rotation of the field lines arises at the border of the foreshock. A distinct discontinuity at  $\alpha = 0$  is seen in all curves. Another noticeable feature is a small decrease of the magnetic field magnitude with increase of the angle  $\alpha$ . A similar trend of rotation of the magnetic field and a gradual decrease of the magnetic field value with increase of the  $\alpha$  angle ( $\alpha > 0$ ) was observed on the third elliptical orbit (February 8, 1989) when the spacecraft approached Mars inside the ion foreshock [Dubinin et al., 1999]. Amplitude of speed variations was small ( $10\text{--}15 \text{ km s}^{-1}$ ) and significant deceleration of the solar wind was recorded only at  $\sim 1500$  km from the bow shock.

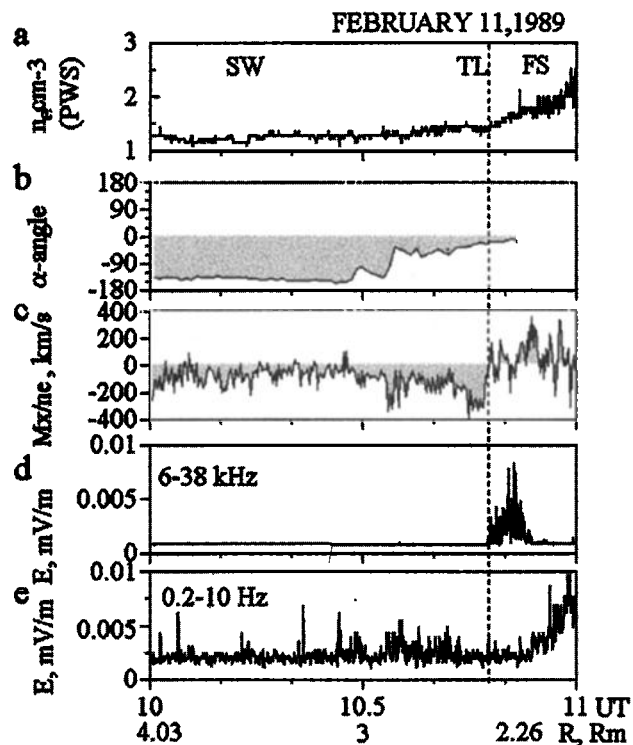


**Figure 5.** (a) The electron number density derived from the potential measurements, (b) the angle  $\alpha$ , (c) the second moment of the electron distribution function divided by the density ( $|V_e| \geq 1500 \text{ km s}^{-1}$ ), and amplitudes of (d) the electron plasma oscillations and (e) low-frequency waves in the elliptical orbit on February 11, 1989.

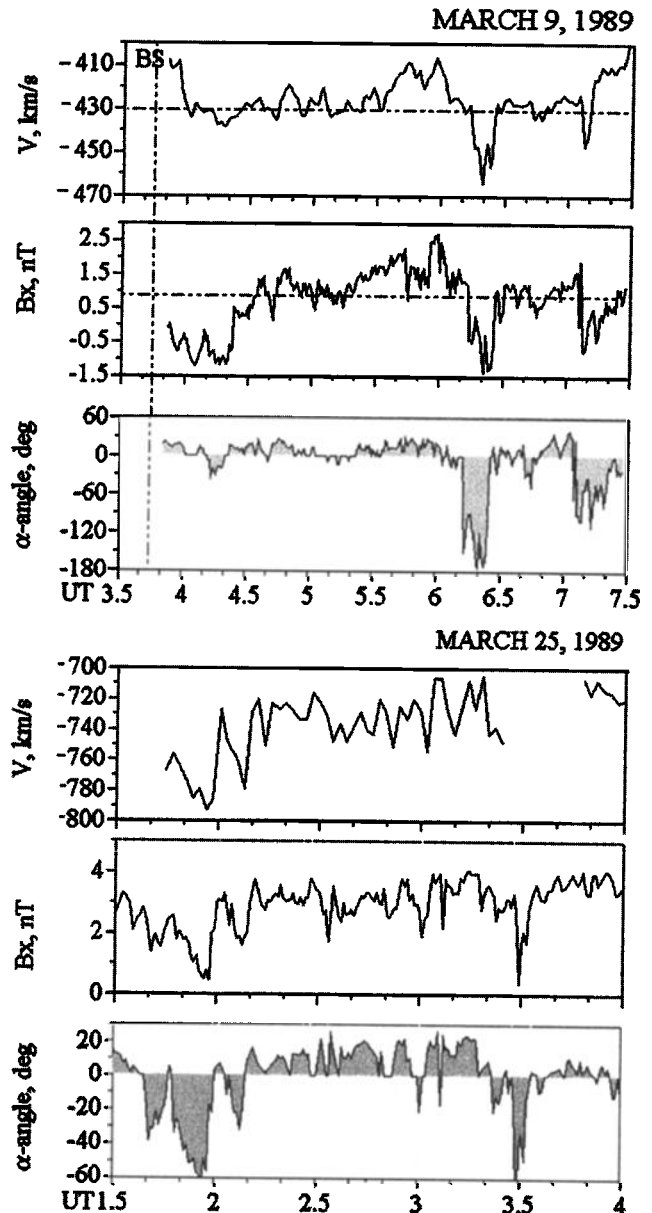


**Figure 6.** Variations of the plasma flow ( $V$ ), the magnetic field ( $B_x$ ), and the angle  $\alpha$  in the upstream region of circular orbits on March 9 and 25, 1989.

On February 11, 1989, the spacecraft approached the planet outside the foreshock. The TAUS instrument did not operate and signatures of the solar wind mass loading could be identified only from the measurements of the floating potential [Pedersen et al., 1991]. The electron number density derived from the potential measurements is shown in Figure 5a. Increase of the electron number density is observed when the spacecraft crosses the tangent line ( $\sim 1047$  UT). The crossing and entry into the electron foreshock is clearly seen from appearance of the electron plasma oscillations (6–38 kHz) and backstreaming electrons ( $M_x > 0$ ). Then, Phobos 2 travels in the region adjacent to the bow shock that is confirmed by significant enhancement of the ULF turbulence (0.2–10 Hz). Spikes of low-frequency waves up-

stream of the tangent line might be of the solar wind origin or be generated by pickup protons that originated from the extended hydrogen corona. It is worth noting that *Barabash* [1991] have detected appearance of pickup protons at 1024 UT.

### 3.2. Circular Orbits

Most of the measurements in the solar wind/foreshock were made on circular orbits ( $R \sim 2.8R_M$ ). The circular orbit was close to the ecliptic plane and provided a good coverage of the region upstream of the bow shock (Figure 1). The observations made on the circular orbits eliminate effects of dependence of plasma and field variations on the planetocentric distance. Figure 6 shows two typical examples of the measurements of the solar wind velocity  $V$ , the component of the magnetic field  $B_x$ , and the angle  $\alpha$ . It is seen that the magnetic field configuration varies significantly and a formal distinction between quasi-perpendicular /quasi-parallel shocks on inbound /outbound legs is ambiguous. The spacecraft is traveling near the tangent line, with frequent excursions from the foreshock to the solar wind. Some transitions are accompanied by distinct increase of the solar wind speed. Correlation between perturbations in flow and magnetic field is obvious. In Figure 7 the solar wind velocity and the magnetic field are plotted versus the angle  $\alpha$  for the orbit on March 25, 1989. The spacecraft was three-axis stabilized, and the reliable measure-

ments of the density variations are available. The velocity decreases with increase of the angle  $\alpha$ . A gradual rotation of the magnetic field vector is observed not only in the foreshock but also in the undisturbed solar wind ( $\alpha < 0$ ), although a distinct fracture at  $\alpha = 0$  in the curves of the magnetic field components and the cone angle  $\varphi$  is seen. The magnitude of the magnetic field and the plasma density do not vary significantly in the solar wind with a trend toward decrease (increase) of the magnetic field magnitude (the proton number density) across the foreshock boundary. All these features give a hint that the foreshock boundary is not simply a topological boundary, which separates the regions either magnetically connected or disconnected with the bow shock. An increase of the proton temperature at factor of two also supports this conclusion.

## 4. Discussion

### 4.1. Mass loading?

Addressing the question concerning probable mass loading features, we compare the observations of the electron number density, derived from the PWS differential potential measurements on the elliptical orbits when the experiment has operated in the biased mode, to the density of pickup ions evaluated from the model assumptions. Figure 8 (bottom) shows the measured electron number density  $n_e$  calculated in the assumption that the mean kinetic energy of the electrons  $T_e = 1$  eV [*Pedersen et al.*, 1991]. Figure 8 (bottom middle) presents the product  $n = n_{\text{exosp}} \cdot (1/\sin\varphi)$ , where  $n_{\text{exosp}}$  is the number density of hydrogen atoms according to the Chamberlain's [1963] model for solar maximum conditions, and  $\varphi$  is the cone angle of the interplanetary magnetic field ( $n_{\text{exosp}} = n_o \exp(H/R - H/R_o) \zeta(R)$ , where  $H = GM_m m_H / kT$ ,  $G$  is gravitation constant,  $M_m$  and  $m_H$  are the masses of Mars and hydrogen atom,  $T$  is the exosphere temperature ( $T=350$  K),  $\zeta(R)$  is the partition function,  $n_o = 3 \cdot 10^4 \text{ cm}^{-3}$  is the number density at  $R = R_o = 250$  km), which is proportional to the number density of pickup ions. Indeed, assuming that pickup protons leave a site of their origin by the  $\mathbf{E} \times \mathbf{B}$  drift, we can estimate their residence time as  $\tau_{\text{res}} \sim L/V_{sw} \sin\varphi$ , where  $L$  is the characteristic scale and  $V_{sw} \sin\varphi$  is the escape velocity. Then, the number density of pickup protons  $n_{\text{pickup}} \sim n_{\text{exosp}} \tau_{\text{res}} / \tau_{\text{ion}} \sim nL / (V_{sw} \tau_{\text{ion}})$ , where  $\tau_{\text{ion}}$  is the ionization time ( $\tau_{\text{ion}} \sim 3 \cdot 10^6$  s), and  $n = n_{\text{exosp}} / \sin\varphi$ . Therefore variations in the IMF direction will cause variations in  $n_{\text{pickup}}$ . A comparison between the observations ( $n_e$ ) and the "model" reveal a similar trend of a gradual increase with some similarities in details that give a hint that the variations in the electron number density derived from floating potential are related to a newly ionized matter of the planetary origin. However, we meet with the obvious problems of getting a quantitative agreement. The residence time  $\tau_{\text{res}} \sim L/V_{sw}$  has to be of  $\sim 2$  orders greater than the derived value for  $L \sim 6000$

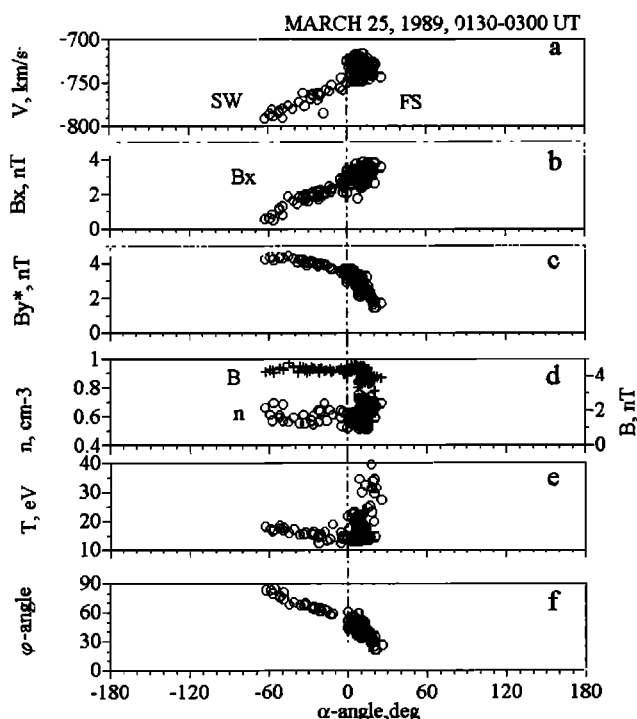


**Figure 7.** Dependence of the plasma and the magnetic field versus the angle  $\alpha$  for the orbit on March 25, 1989. (a) The bulk velocity of the solar wind  $V$ , (b and c) the components  $B_x, B_{y*}$ , (d) the magnetic field value  $B$  and the proton number density  $n$ , (e) the proton temperature  $T$ , and (f) the cone angle  $\varphi$ .

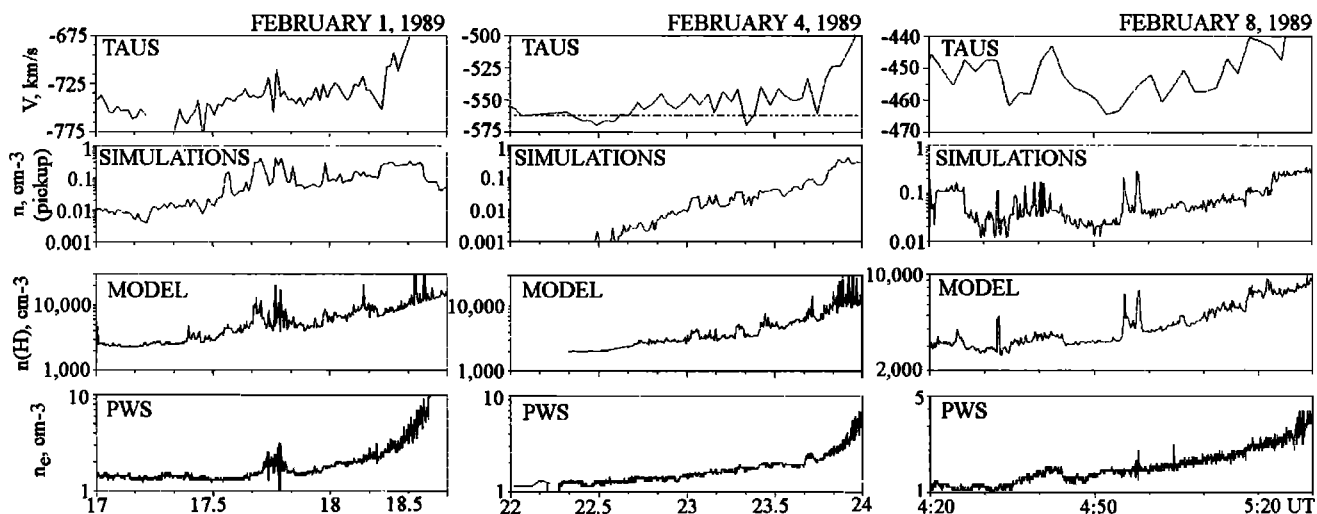


**Figure 8.** (top) Proton bulk velocity, (top middle) the number density of pickup protons derived in the test particle simulations (curves labeled as "simulations"), (bottom middle) the "effective" number density of hydrogen atoms (curves labeled as "model"), and (bottom) the electron number density evaluated from the difference potential measurements (February 1, 4, and 8, 1989).

km,  $V_{sw} \sim 500 \text{ km s}^{-1}$ . The agreement can be improved by a factor of 10 if we take into consideration a specular reflection of pickup ions at the bow shock. Reflection of protons leads to their redistribution controlled by the magnetic field orientation. The bunch of reflected pickup protons guided by the IMF is localized in the foreshock and provides a distinct asymmetry in the density of pickup protons [Dubinin et al., 1994a]. The curves shown in Figure 8 (top middle) give the distribution of pickup protons from the test particle model. In the simulations, ion trajectories of 50,000 test particles in the external electric ( $\mathbf{E} = -1/c\mathbf{V}_{sw}\times\mathbf{B}$ ) and the magnetic field  $\mathbf{B}$  taken from the measurements were calculated. Test particles are weighted in accordance to the exosphere profile of hydrogen atoms. The family of distributions of the proton number density was evaluated for different cone angles to get the number density along the real spacecraft trajectory. It is seen that the "memory" about original  $\varphi$  angles of pickup ions is conserved and therefore variations in  $n_i$  ("simulation" curves) replicate many features in  $n$  (model curves). An additional factor of 10 can be found by assuming a denser hydrogen atmosphere. It is worth noting that Dubinin et al. [1994a] have used the value  $n_o = 2 \cdot 10^5 \text{ cm}^{-3}$  to get a better agreement with the PWS measurements. However, according to the model by [Krasnopolsky and Gladstone, 1996], such values correspond to mean solar activity. The calculated hot oxygen densities are also smaller and do not contribute significantly to the number density of pickup ions [Kim et al., 1998]. From this point of view, a significant growth in the electron number density  $n_e$  while approaching the planet, which is a by-product of the differential potential measurements, remains a puzzle. Probably, electrons accelerated and reflected at the bow shock in-

crease the mean energy of electrons collected by the electric probe and modify the floating potential.

Figures 9a-9c show the bulk speed versus the "effective" number density  $n$  (the number density of neutral hydrogen atoms  $n_{\text{exosp}}$  multiplied by factor of  $1/\sin\varphi$ ) for three elliptical orbits. Figure 9d presents the planetocentric distance  $R$  evaluated from the effective number density according to the equation  $n = n_o \exp(H/R - H/R_o)$ . In other words, to adjust the data to similar IMF conditions in the solar wind ( $\varphi = 90^\circ$ ), variations in  $n$  caused by changes in the cone angle  $\varphi$  are transformed to the dependence on  $R$ . As seen from figure 9a (February 1, 1989), a gradual deceleration starts at distance of  $\sim 9000 \text{ km}$ . The decrement reaches  $25\text{-}30 \text{ km s}^{-1}$  at  $\sim 6000 \text{ km}$ . Then, the efficiency of deceleration strongly increases. The decrease in speed reaches  $\sim 200 \text{ km s}^{-1}$  at  $\sim 4700 - 5000 \text{ km}$ . On February 4, 1989 (Figure 9b), the solar wind slightly slows down at  $R \sim 6000 \text{ km}$  with significant braking at  $\sim 5000 \text{ km}$ . In the third orbit, deceleration is visible only at  $R \sim 6000 \text{ km}$  with a peculiar splitting on two curves with small and large slopes. A splitting is also seen in the curves for the orbits on February 1 and 4. Different values of the velocity are observed for the same number density of thermal hydrogen corona and the same inferred distance  $R$ . The splitting in the velocity curves appears because the points come from different locations along the spacecraft orbit in accordance to different cone angles and residence times of newly born ions. Then, two different sources of neutral populations (e.g. hydrogen and oxygen) might provide a peculiar splitting of mass loading efficiency. The curves with a lower decrement of the velocity could be related to mass loading on hydrogen corona, whereas the curves with a larger decrement give a hint of mass loading on oxy-

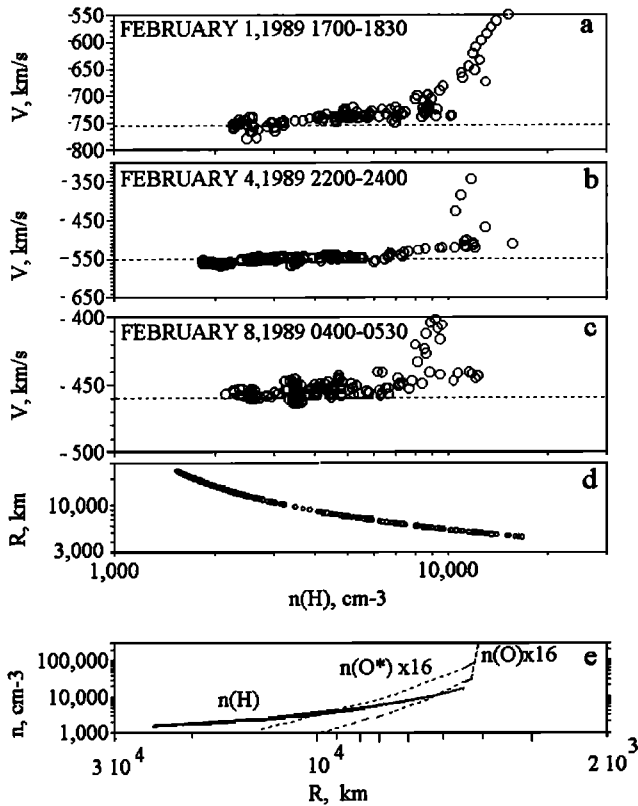


**Figure 9.** (a-c) Dependence of the bulk speed versus the effective number density  $n$  (the number density of hydrogen atoms  $n_{\text{exosp}}$  multiplied by factor  $1/\sin\varphi$ ). Dashed horizontal lines are given for the reference. (d) The distance  $R$  to the planet, which corresponds to the values of the effective number density. (e) The number density of hydrogen and oxygen atoms versus the distance  $R$ . The solid curve is the number density of hydrogen atoms. Dashed lines at  $R > 4000$  km show the density of hot oxygen ( $O^*$ ) atoms multiplied by factor of 16. The upper and lower dashed lines correspond to the extreme and solar maximum conditions [Ip, 1990]. The dashed line at  $R < 4000$  km is the number density ( $\times 16$ ) of "cold" oxygen atoms.

gen atmosphere. Indeed, according to the models, at the distances of  $\sim 5000 - 6000$  km the mass density of atmospheric oxygen begins to dominate over hydrogen. Figure 9e presents the mass number density of hydrogen and oxygen atoms versus the planetocentric distance  $R$ . Solid line shows the mass number density of hydrogen atoms. Dashed lines at  $R > 4200$  km give the mass density of oxygen ( $O^*$ ) atoms, originated from hot oxygen corona (the number density multiplied by factor of 16). The upper and lower dashed lines correspond to the extreme and solar maximum conditions [Ip, 1990]. Dashed line at  $R < 4200$  km gives the number density ( $\times 16$ ) of "cold" atmosphere oxygen atoms. A fracture in the curve of the total mass number density of neutrals (not shown in Figure 9) is easily recognized.

Although the mass loading mechanism of the solar wind deceleration seems to be attractive, we meet with several serious observational and theoretical problems.

Unlike the comet case, there is not enough room near Mars for quick assimilation of pickup ions and effective mass loading. The characteristic scale of pitch angle diffusion of exospheric protons (the scale of assimilation into the solar wind flow due to scattering on low-frequency wave turbulence) is  $\sim 15R_M$  [Barabash *et al.*, 1991]. For oxygen ions with gyroradius of  $\sim 8R_M$ , we even meet with more serious problems applying the MHD approach for description of mass loading. A kinetic approach, which is more appropriate for the Mars conditions, assumes that the momentum transfer is most efficient in the case where the IMF is in the perpendicular direction with respect to the X axis ( $\varphi \sim 90^\circ$ ). However, the observations show that deceleration becomes stronger with decrease of the cone angle  $\varphi$ . One may expect also that solar wind mass loading should be accompanied by increase of the cross-flow component of the magnetic field in the subsolar region. On the contrary, increase of the  $B_x$  component and decrease of the cross-flow  $B_{y*}$  component with decrease of the solar wind speed is observed. One might expect that mass loading result in at least a weak enhancement of the field value. On the contrary, the observations indicate the opposite trend.

#### 4.2. Alfvén Waves

Correlation between perturbations in flow and magnetic field indicate at a transient origin of the deceleration events. For example, in large-amplitude Alfvén waves perturbations of the velocity  $\mathbf{v}$  and the magnetic field  $\mathbf{b}$  are closely related and follow Walén's relation  $\mathbf{v} = \pm \mathbf{b}/(4\pi\rho)^{1/2} = \pm K_A \mathbf{b}$ , where  $\rho$  is the plasma mass density,  $K_A = 1/(4\pi\rho)^{1/2}$ . Addressing the question of whether the observed events are transient and caused by Alfvén waves propagating in the solar wind, we compared the field and the velocity variations. In most cases, the perturbations in the  $V_x$  and  $B_x$  components are well correlated. Figure 10 shows a relationship between the  $v_x$  and  $b_x$  components measured upstream of the bow shock on three elliptical orbits (February 1, 4, and 8, 1989). It is worth noting that we neglect the solar wind aberration and assume that  $V_x = V$ . A linear dependence of  $v_x = K b_x$  with  $K = 15 \text{ km nT}^{-1} \text{ s}^{-1}$  and  $16.7 \text{ km nT}^{-1} \text{ s}^{-1}$  is observed in the elliptical orbits on February 1 and 4, respectively. The factor  $K_A = 22/n^{1/2} \text{ km nT}^{-1} \text{ s}^{-1}$  ( $n$  is the plasma number density) expected for Alfvén waves [Belcher and Davis, 1971] is well fitted with the observations ( $K_A = 15.6$  ( $n = 2 \text{ cm}^{-3}$ ) and  $K_A = 16.9$  ( $n = 1.7 \text{ cm}^{-3}$ ), respectively). Perturbations in the solar wind speed occur more at random on February 8, and identification of Alfvén waves seems rather ambiguous although the values of  $K$  and  $K_A$  are nearly equal ( $K = 14.6$ ,  $K_A = 16.9$ ). The important point is that in all elliptical orbits, perturbations in flow and magnetic field observed at planetocentric distances  $R \leq 6000$  km do not follow the Walén relation. In Figure 11 a relationship between the perturbations of velocity and magnetic field on two

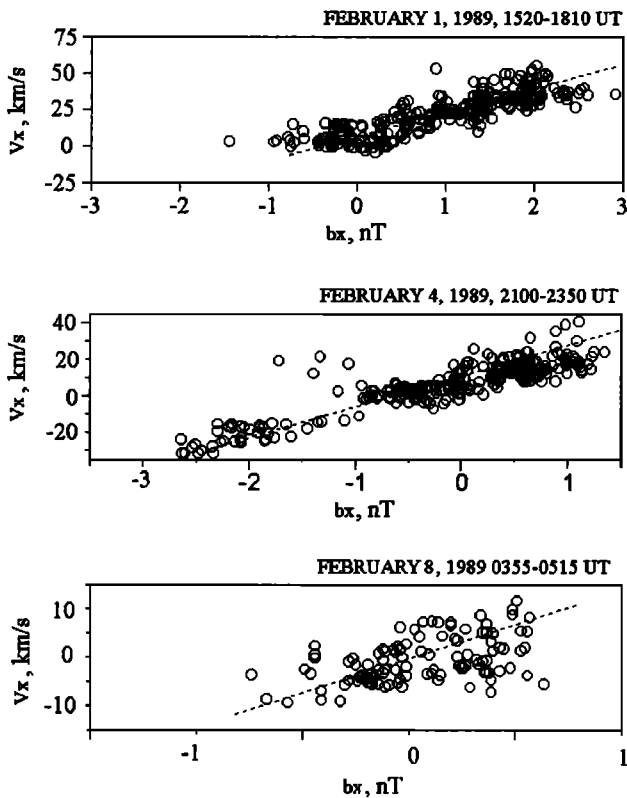


**Figure 10.** Relationship between the  $v_x$  and  $b_x$  components of the perturbations measured upstream of the bow shock on three elliptical orbits (February 1, 4, and 8, 1989).

circular orbits is plotted. A linear dependence between the perturbations with the coefficient of  $K = 13$  close Alfvén wave factor ( $K_A = 15$ ) suggests the wave origin of the variations observed on March 9, 1989. The relationship between  $v_x$  and  $b_x$  perturbations on March 25, 1989, is also close to the linear one with  $K = 27.8$  ( $K_A = 28.9$ ).

In Walén's relation a plus (minus) sign is taken as sign of the product  $(-\mathbf{k}\mathbf{B}_0)$  and varies in dependence on the wave propagation vector  $\mathbf{k}$  with respect to the ambient magnetic field  $\mathbf{B}_0$ . The in-phase relationship between perturbations in velocity and magnetic field observed in all previous events suggests an antisunward direction of wave propagation. An Alfvén wave traveling in the antisunward direction, opposite to the IMF, perturbs the field and the solar wind velocity with an in-phase relationship between  $v$  and  $b$ . If the perturbation  $b_x > 0$ , the tangent line turns from its nominal position shown by the solid arrow TL and appears in the location 1 (Figure 12). Then, an observer at point  $O$  occurs in the foreshock and records a decrease of the solar wind velocity ( $|\mathbf{V}_0 + \mathbf{v}| < |\mathbf{V}_0|, \mathbf{V}_0 < 0, \mathbf{v} > 0$ ). For the perturbation with  $b_x < 0$  ( $v_x < 0$ ) the tangent line goes to the location 2 and the observer arrives in the solar wind ( $\alpha < 0$ ). The perturbed velocity  $|\mathbf{V}_0 + \mathbf{v}| > |\mathbf{V}_0|$  increases. Thus the observations in the undisturbed solar wind ( $\alpha < 0$ ) of ascending tones in the  $B_x(\alpha)$  di-

agrams (see, for example, Figure 7) are easily explained by large-amplitude Alfvén waves propagating in the solar wind. The magnitude of the magnetic field and the plasma density do not vary significantly in the solar wind, which also supports our suggestion that the variations in the field direction and the solar wind velocity are controlled by Alfvén waves.

A similar pattern could be expected if large-amplitude Alfvén waves are generated at or near the foreshock boundary. The only difference is that disturbances would be localized in the region adjacent to the tangent line. The scheme shown in Figure 12(top) illustrates appearance of acceleration/deceleration events near the tangent line. The interesting effect is that the sign of perturbations is opposite near the foreshock boundary located downstream with respect to the tangent point. Figure 12 (bottom) gives the example of the measurements made near both segments of the tangent line, upstream and downstream relative to the tangent point. The solar wind speed, the amplitude of electron plasma emissions, the angle  $\alpha$ , and antisunward/sunward anisotropy of fluxes of suprathermal electrons are shown. The upstream edge of the electron foreshock is clearly identified at 1823 UT by the onset of electron plasma waves, change of signs of the angle  $\alpha$ , and anisotropy of electron fluxes. A crossing of the tangent line downstream with respect to the tangent point occurs at  $\sim 1959$  UT. At the upstream crossing, the plasma accelerates upstream of the tangent line and decelerates downstream. The opposite sequence of the events is observed at the second crossing, downstream of the tangent point. Slow down of the solar wind at 1930-2000 UT is followed by plasma acceleration. Similar acceleration/deceleration events accompanying by bipolar variations of the magnetic field are often observed near the tangent line [Dubinin et al., 1999]. Bipolar variations of the magnetic field centered at the

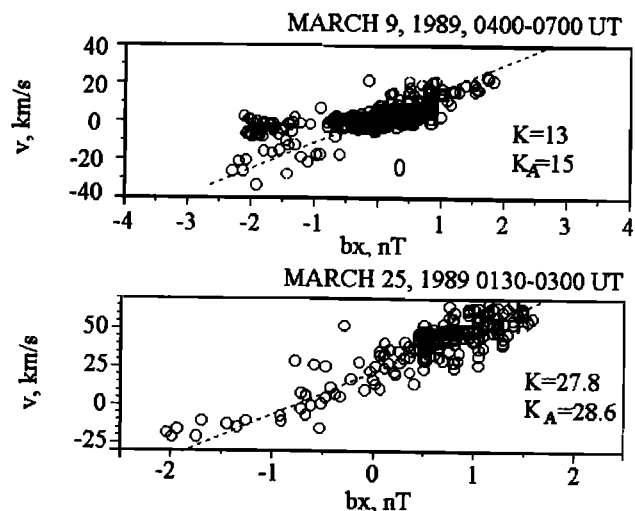


**Figure 11.** Relationship between the  $v_x$  and  $b_x$  components measured upstream of the bow shock on two circular orbits (March 9 and 25, 1989).

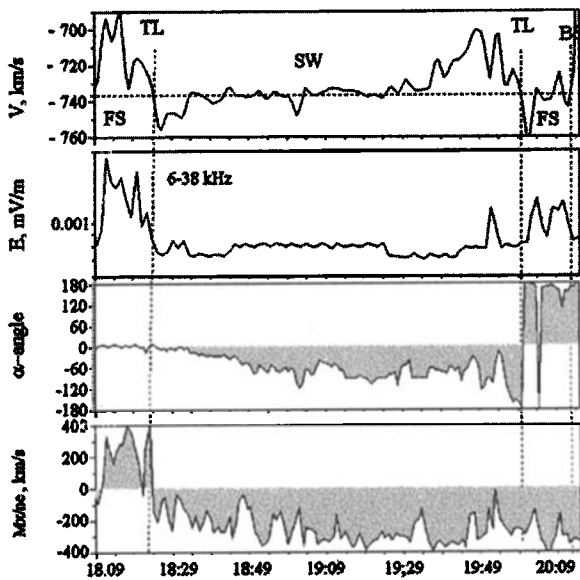
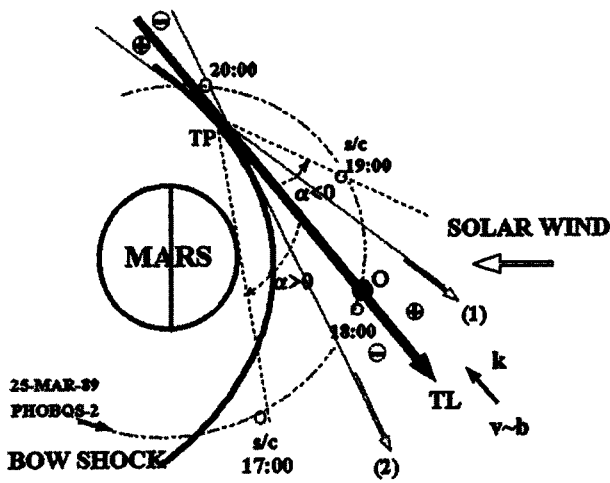


**Figure 12.** (top) Projection of the circular orbit on March 25, 1989, onto the XY plane (MSO reference frame) and the average position of the tangent line (solid line). Plus/minus signs show regions adjacent to the tangent line where an increase/decrease of the solar wind velocity is observed. (bottom) The proton velocity  $V$ , the intensity of the electron plasma oscillations, the angle  $\alpha$ , and sunward/antisunward anisotropy of suprathermal electrons  $M_x/n_e$ .

plane normal to the tangent surface and intersected the bow shock at tangent points were also reported by [Dubinin et al., 1998a]. In this paper we suggest that such signatures are time-varying perturbations propagating in the solar wind or generated at/near the foreshock boundary. Indeed, according to the scheme shown in Figure 12, sign of variations in the  $\Delta B_x (\Delta B_{y*})$  component changes across  $\alpha \sim -90^\circ$ .

If the proposed interpretation that perturbations of the magnetic field and the solar wind velocity are mainly caused by propagating Alfvén waves is correct, the structure of the solar wind/foreshock interface must be

reversed in case of waves traveling in the opposite direction, toward the Sun. In such waves the  $v$  and  $b$  perturbations are anticorrelated, and one would expect increase of the solar wind velocity in the upstream foreshock as compared to the undisturbed solar wind speed. Schemes, shown in Figure 13, illustrate expected variations of the solar wind speed near the tangent line in cases of Alfvén waves propagating in antisunward (Figure 13a) and sunward (Figure 13b) directions. We found several orbits with sunward traveling waves. Figure 14 presents the example of the observations in circular orbit on March 10, 1989. Contrary to previous events, the perturbations of the flow and the magnetic field are anticorrelated, which is clearly seen from the  $v_x - b_x$  re-

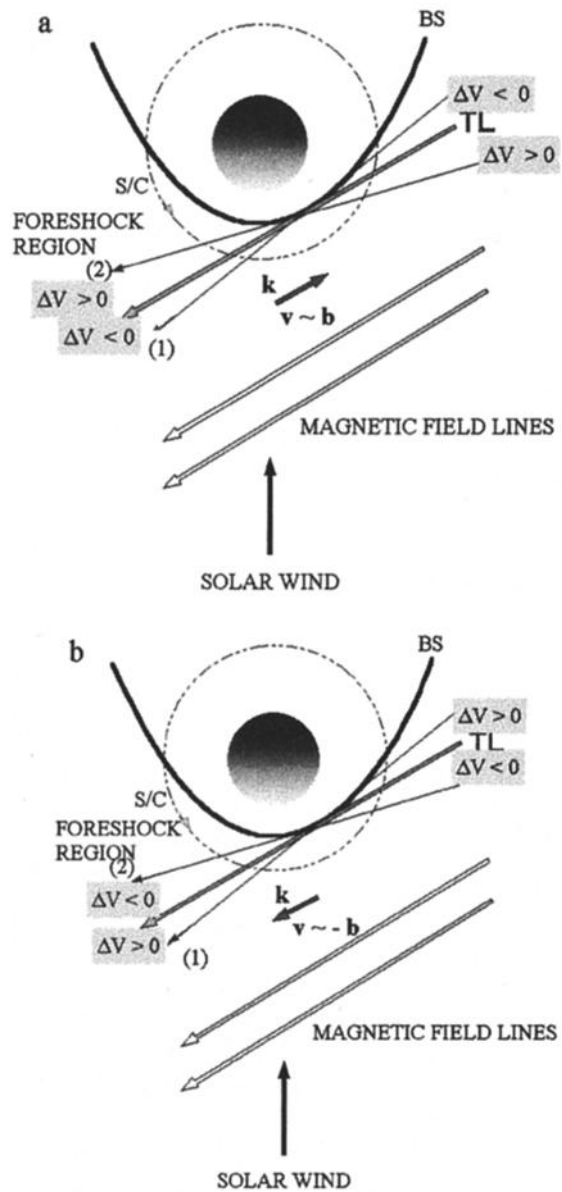


**Figure 13.** Schemes illustrating the effect of Alfvén waves perturbations propagating in (a) antisunward and (b) sunward directions. The structure of the solar wind/foreshock interface is reversed in dependence on the direction of wave propagation.

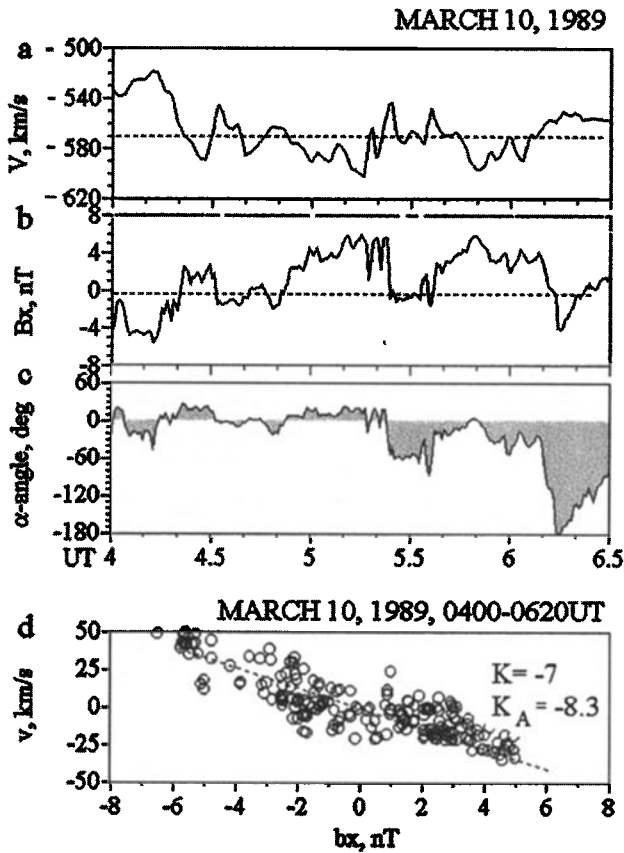


**Figure 14.** Variations of (a) the plasma flow ( $V$ ), (b) the magnetic field ( $B_x$ ), and (c) the angle  $\alpha$  in the upstream region of circular orbit on March 10, 1989. Dashed-dotted horizontal lines drawn to indicate average values give the undisturbed parameters of the velocity and the magnetic field, although some uncertainty remains in this procedure. (d) A relationship between the perturbations of flow and magnetic field.

relationship shown in Figure 14b. The spacecraft records a decrease of the proton velocity when it occurs in the solar wind ( $\alpha < 0$ ). The velocity increases while the spacecraft entering the foreshock ( $\alpha > 0$ ). This test strongly supports our suggestion that large-amplitude Alfvén waves control the perturbations of the plasma and the IMF near the tangent line.

Perturbations can be provided either by waves of the solar wind origin or by waves excited in the foreshock or near its boundary. The schematic shown in Figure 15 gives a dependence  $V(\alpha)$  which might be observed under action of different sources of perturbations. Figure 15 (top right) corresponds to the case of Alfvén wave with a hump in the speed that moves the tangent line from (TP1) to (TP2). Passage of the wave gives an increasing tone in the diagram. Figure 15 (top middle right) corresponds to the case when the bipolar perturbation is excited near the foreshock boundary, and disturbances are localized in the neighborhood of the tangent line. Figure 15 (bottom middle right) shows a dependence  $V(\alpha)$  expected, for example, at shock-like

transition. Figure 15 (bottom right) presents a combined effect of all above sources. Figure 16 shows the examples of the measurements made on several circular orbits. Figure 16 (top and top middle) hint at the presence of Alfvén waves in the solar wind. Figure 16 (bottom middle and bottom) indicate excitation of Alfvén waves and/or shock-like transition at the tangent line. In all cases, a change of a slope and enhancement of a scattering of the data points near  $\alpha = 0$  show more complicated structure of the solar wind/foreshock interface as compared to purely Alfvén waves of the solar wind origin which only change the position of the tangent line. Variations of the number density and the magnetic field value across the foreshock show the existence of compressional modes. Decrease of the magnetic field and increase of the number density hint at excitation of slow modes. It is interesting to note that sign of "refraction" of the magnetic field lines at  $\alpha = 0$  is fitted with a slow mode transition if we interpret the observations in terms of a steady model. However, we cannot infer whether or not compressive modes are switched on by Alfvén waves striking the foreshock or are driven by local processes of the solar wind/foreshock interaction. Theoretical studies [McKenzie and Westphal, 1969; Lin et al., 1996] showed that the interaction of an Alfvén wave with the bow shock results in amplification of the Alfvén wave, as well as generation of slow mode in the downstream region. Although this conclusion is not applied in a direct manner to Alfvén waves striking the foreshock, the data indicate that similar processes may take place at the foreshock boundary. On the other hand, we have also evident examples when Alfvén waves are observed only when the spacecraft crosses the tangent line. It is important to note that rotation of the magnetic field at/near the tangent line occurs out of the plane containing the  $V_{sw}$  and  $B_{sw}$  vectors. Figure 17 shows cross-flow component of the field in the YZ plane of the Mars solar orbital (MSO) reference frame (the Y axis opposes to the direction of the planetary

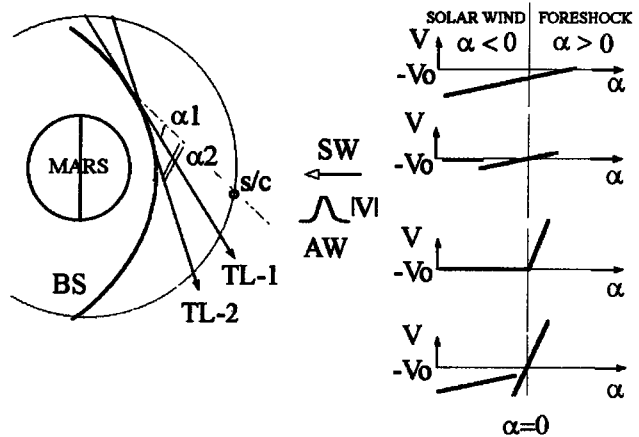


**Figure 15.** Schematic of the  $V(\alpha)$  curves expected under different assumptions about the source of the perturbations.

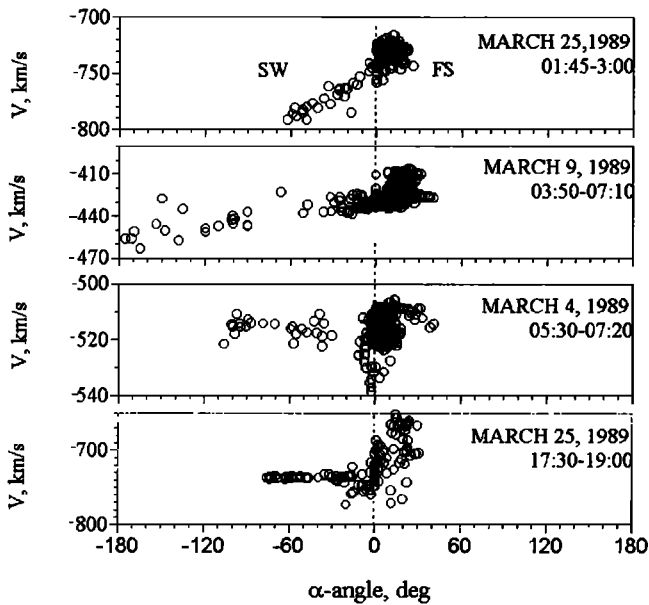


**Figure 16.** The examples of the observed variations  $V(\alpha)$  in circular orbits.

motion and the  $Z$  axis points to the north) across the tangent line for the elliptical and the circular orbits. A distinct rotation of the magnetic field is observed near the tangent line where a clock angle suddenly varies by  $\sim 90^\circ$ .

*Kotova et al.* [1997] have analyzed a relationship between the velocity decrement upstream of the Martian bow shock and the number density of the solar wind and have found an inverse relation  $\delta v \sim 1/n_{sw}$ . They exploited this fact as the main argument in favor of the mechanism deceleration associated to mass loading on oxygen and hydrogen coronas. We note that Alfvén waves can also lead to the inverse dependence between the velocity perturbations and the number density ( $\delta v \sim 1/\sqrt{n_{sw}}$ ). It is believed that the events observed at distances  $R > \sim 6000$  km are manifestations of large-amplitude Alfvén waves generated or amplified at/near the foreshock boundary. A visible relation (Figure 9) between the velocity decrement  $\Delta V_{sw}$  and the density of pickup ions ( $\sim n_{exosp}/\sin\varphi$ ) is revealed because both values depend on the magnetic field orientation controlled by Alfvén waves. Large-amplitude waves with  $\Delta B_x > 0$  increase the residence time of newly born exospheric/atmospheric ions and may be responsible for the observed perturbations in the floating potential. It is worth noting that a cause-and-effect relation between Alfvén waves and pickup ions probably is more complicated, and the question of whether Alfvén waves are triggered by reflected pickup ions should be addressed. Indeed, in many cases, waves and mass loading features from the floating potential measurements are observed only in the foreshock. However, we cannot infer from the data a direct evidence of cause-and-effect relation between both phenomena, and simultaneous three-

dimensional measurements of the ion fluxes as well as hybrid simulations of the curved bow shock with inclusion of pickup ion population are necessary. The question of whether or not generation of large-amplitude Alfvén and compressional modes within the Martian foreshock is a common feature of planetary foreshocks also requires a special comparative study. We want only to note that deceleration in the Earth’s foreshock is correlated with “diffuse” backstreaming ions whose number density is about 1–3% of the ambient solar wind density [Gosling et al., 1982]. A typical decrement of the solar wind velocity is about 7–10 km s<sup>-1</sup> [Bame et al., 1980], although much higher values ( $\sim 40$  km s<sup>-1</sup>) are also reported [see, e.g., Zhang et al., 1997, Figure 4].

We assume that mass loading effects at Mars may be essential only at closer distances to the planet ( $R \leq 6000$  km) where the decrement of the speed strongly increases and Walén’s relation between the plasma and field perturbations is violated. At these distances the mass number density of pickup ions is not too small, and mass loading may occur through the macroscopic electromagnetic fields caused by a differential streaming of ions [Omidi and Winske, 1987; Sauer et al., 1998; Dubinin et al., 1998b]. A strong deceleration of the solar wind protons is provided by the Lorentz force ( $\sim \Delta \mathbf{V} \times \mathbf{B}$ ), which arises due to relative motion of the solar wind protons and oxygen ions. On the circular orbits, where the spacecraft was far from the planet ( $R \sim 10^4$  km), a reliable recognition of deceleration features caused by mass loading, even in the absence of large-amplitude Alfvén waves, is ambiguous.

### 5. Summary

Multi-instrument data analysis of the observations made by the Phobos 2 spacecraft in the upstream Mar-

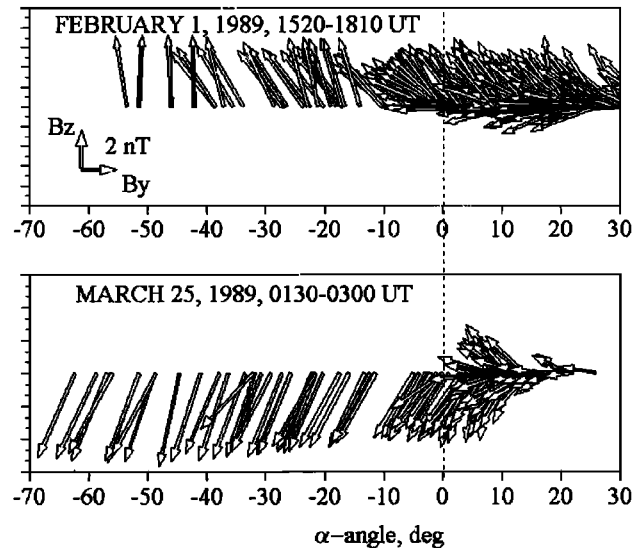


**Figure 17.** Projections of the magnetic field onto the  $YZ$  plane in the MSO coordinates versus the angle  $\alpha$  for two typical elliptical and circular orbits.

tian environment is performed. It is shown that the solar wind deceleration observed in elliptical and circular orbits and previously referred to as mass loading by planetary exosphere occurs mainly in the foreshock region. The boundary of the foreshock is reliably identified from the model calculations and the observations of the electron plasma oscillations and sunward fluxes of suprathermal electrons. The flow and field variations follow Walen's relation that suggests their Alfvén wave origin. Phase relationship between the perturbations of the velocity and the magnetic field indicates an anti-sunward direction of wave propagation. Owing to large amplitude perturbations of the magnetic field orientation in Alfvén waves, the solar wind/foreshock interface is very dynamic, something that is displayed in frequent excursions of the spacecraft from the solar wind to the foreshock and back. The sign of the perturbation in the velocity corresponds to decrease of the solar wind speed while the spacecraft goes into the foreshock. The structure of the interface downstream with respect to the tangent point occurs in the opposite direction. The interpretation of the observed events as Alfvén waves is verified by the observations of sunward propagating waves. Alfvén waves traveling toward the Sun reverse the sense of the interface pattern with acceleration signatures across the tangent line. The flow and field variations can be provided either by waves of the solar wind origin or by waves excited in the foreshock or near its boundary. It is found that both mechanisms contribute to the observed features. However, even in the first case, the observations show that the foreshock boundary is not simply a topological boundary separating the regions either magnetically connected or disconnected with the bow shock. The transition across the tangent line is often accompanied with a sharp change of the clock angle of the magnetic field, a decrease of the magnetic field value, and an increase of the proton number density and temperature. Although variations of the solar wind speed at  $R \geq 6000$  km are controlled by Alfvén waves generated within the foreshock or at its boundary, we can not exclude a cause-and-effect relation between Alfvén waves and large fluxes of reflected pickup protons. At closer distances to the planet ( $R \leq 6000$  km) where the solar wind slows down at 150-200  $\text{km s}^{-1}$  perturbations of the field and velocity do not follow the Walen relation. This strong deceleration hints at mass loading on an oxygen atmosphere.

**Acknowledgments.** Michel Blanc thanks Christian Mазelle and another referee for their assistance in evaluating this paper.

## References

- Bame, S. J., J. R. Asbridge, W. C. Feldman, J. T. Gosling, G. Paschmann, and N. Sckopke, Deceleration of the solar wind upstream from the Earth's bow shock and the origin of diffuse upstream ions, *J. Geophys. Res.*, **85**, 2981, 1980.
- Barabash, S., E. Dubinin, N. Pissarenko, R. Lundin, and C. T. Russell, Picked-up protons near Mars: Phobos observations, *Geophys. Res. Lett.*, **18**, 1805, 1991.
- Barabash, S., and R. Lundin, Reflected ions near Mars, Phobos-2 observations, *Geophys. Res. Lett.*, **20**, 787, 1993.
- Belcher, J. W., and L. Davis Jr., Large-amplitude Alfvén waves in the interplanetary medium, **2**, *J. Geophys. Res.*, **76**, 3534, 1971.
- Bonifazi, C., G. Moreno, A. J. Lazarus, and J. D. Sullivan, Deceleration of the solar wind in the Earth's foreshock region: ISSE 2 and IMP 8 observations, *J. Geophys. Res.*, **85**, 6031, 1980.
- Brecht, S. H., Hybrid simulations of the magnetic topology of Mars, *J. Geophys. Res.*, **102**, 4743, 1997a.
- Brecht, S. H., Solar wind deposition into the Martian atmosphere, *J. Geophys. Res.*, **102**, 11,287, 1997b.
- Chamberlain, J. W., Planetary coronae and atmospheric evaporation, *Planet Space Sci.*, **11**, 901, 1963.
- Delva, M., U. Nischelwitzer, and K. Schwingenschuh, Despinning and Tests of the MAGMA data in orbits around Mars, *Report IWF 9407*, Space Research Institute, Graz, Austria, 1994.
- Delva, M., and E. Dubinin, Upstream ULF fluctuations near Mars, *J. Geophys. Res.*, **103**, 317, 1998.
- Dubinin, E., D. Obod, A. Pedersen, and R. Grard, Mass loading asymmetry in the upstream region near Mars, *Geophys. Res. Lett.*, **21**, 2769, 1994a.
- Dubinin, E., R. Lundin and K. Schwingenschuh, Solar wind electrons as tracers of the Martian magnetotail topology, *J. Geophys. Res.*, **99**, 21,233, 1994b.
- Dubinin, E., D. Obod, R. Lundin, K. Schwingenschuh, and R. Grard, Some features of the Martian bow shock, *Adv. Space Research*, **15**(8/9), 423, 1995.
- Dubinin, E., and R. Lundin, Mass-loading near Mars, *Adv. Space Res.*, **16**(4), 75, 1995.
- Dubinin, E., K. Sauer, M. Delva, and A. Skalsky, The IMF bending upstream of the Martian bow shock, *Earth Planets Space*, **50**, 289, 1998a.
- Dubinin, E., K. Sauer, K. Baumgartel, and K. Srivastava, Multiple shocks near Mars, *Earth Planets Space*, **50**, 279, 1998b.
- Dubinin, E., K. Sauer, M. Delva, S. Livi, A. Skalsky, and K. Szego, Deceleration of the solar wind upstream of the Martian bow shock. Mass loading or foreshock features?, *Adv. Space Res.*, *in press*, 1999.
- Gosling, J. T., M. F. Thomsen, S. J. Bame, W. C. Feldman, G. Paschmann and N. Sckopke, Evidence for specularly reflected ions upstream from the quasiparallel bow shock, *Geophys. Res. Lett.*, **9**, 1333, 1982.
- Grard, R., D. Klinge, S. Klimov, S. Savin, and J.-G. Trotignon, The Plasma Wave System on Phobos, *J. Phys. E. Sci. Instrum.*, **22**, 888, 1989a.
- Grard, R., A. Pedersen, S. Klimov, S. Savin, A. Skalsky, J.-G. Trotignon, and C. Kennel, First measurements of plasma waves near Mars, *Nature*, **341**, 607, 1989b.
- Grard, R., et al., Plasma and waves around Mars, *Planet. Space Sci.*, **39**, 89, 1991.
- Ip, W.-H., On hot oxygen corona at Mars, *Icarus*, **76**, 135, 1988.
- Ip, W.-H., The fast atomic oxygen corona extent of Mars, *Geophys. Res. Lett.*, **17**, 2289, 1990.
- Ip, W.-H., Neutral particle environment of Mars: The exosphere-plasma interaction effects, *Adv. Space Res.*, **12**(9), 205, 1992.
- Kim, J., A. F. Nagy, J. L. Fox, and T. E. Cravens, Solar cycle variability of hot oxygen atoms at Mars, *J. Geophys. Res.*, **103**, 29,339, 1998.
- Kirsch, E., et al., Pickup ions ( $E_{O^+} > 55$  keV) measured near Mars by Phobos-2 in February/March 1989, *Annal. Geophys.* **9**, 761, 1991.

- Kotova, G., et al., Study of the solar wind deceleration upstream of the Martian terminator bow shock, *J. Geophys. Res.*, *102*, 2165, 1997.
- Krasnopolsky, V. A., and G. R. Gladstone, Helium on Mars: EUV and Phobos data and implications for Mars's evolution, *J. Geophys. Res.*, *101*, 15,765, 1996.
- Lammer, H., and S. J. Bauer, Nonthermal atmospheric escape from Mars and Titan, *J. Geophys. Res.*, *96*, 1819, 1991.
- Lin, Y., L. C. Lee, and M. Yan, Generation of dynamic pressure pulses downstream of the bow shock by variations in the interplanetary magnetic field orientation, *J. Geophys. Res.*, *101*, 479, 1996.
- Lundin R., et al., The ASPERA experiment on the Soviet Phobos spacecraft, *Solar System Plasma Physics*, Geophys. Monogr. Ser., vol. 54, edited by J. H. Waite and T. E. Moore, pp. 417-424, AGU, Washington, D. C., 1989.
- McKenzie, J. F., and K. O. Westphal, Transmission of Alfvén waves through the Earth's bow shock, *Planet. Space Sci.*, *17*, 1029, 1969.
- Nagy, A. F., and T. E. Cravens, Hot oxygen atoms in the upper atmosphere of Venus and Mars, *Geophys. Res. Lett.*, *15*, 433, 1988.
- Nagy, A. F., J. Kim, and T. E. Cravens, Hot hydrogen and oxygen atoms in the upper atmospheres of Venus and Mars, *Ann. Geophys.*, *8*, 251, 1990.
- Neugebauer, M., Spacecraft observations of the interaction of active comets with the solar wind, *Rev. Geophys.*, *28*, 231, 1990.
- Omidi, N., and D. Winske, A kinetic study of solar wind mass loading and cometary bow shocks, *J. Geophys. Res.*, *92*, 13,409, 1987.
- Pedersen, A., C. Nairn, R. Grard, and K. Schwingenschuh, Deviation of electron densities from differential potential measurements upstream and downstream of the bow shock and in the magnetosphere of Mars, *J. Geophys. Res.*, *96*, 11,243, 1991.
- Riedler, W., et al., Magnetic fields near Mars: First results, *Nature*, *341*, 604, 1989.
- Rosenbauer, H., et al., Ions of martian origin and plasma sheet in the Martian magnetotail: Initial results of TAUS experiment, *Nature*, *341*, 612, 1989.
- Russell, C. T., J. G. Luhmann, K. Schwingenschuh, W. Riedler, and Y. Yeroshenko, Upstream waves at Mars: Phobos observations, *Geophys. Res. Lett.*, *17*, 897, 1990.
- Sauer, K., E. Dubinin, and K. Baumgartel, Nonlinear MHD-waves and discontinuities in the Martian magnetosheath. Observations and MHD simulations, *Earth Planets Space*, *50*, 793, 1998.
- Sauer K., E. Dubinin, M. Dunlop, K. Baumgartel, and V. Tarasov, Low-frequency electromagnetic waves near and below the proton cyclotron frequency at the AMPTE Ba release: Relevance to comets and Mars, *J. Geophys. Res.*, *104*, 6763, 1999.
- Skalsky, A., et al., The Martian bow shock: wave observations in the upstream region, *J. Geophys. Res.*, *92*, 2927, 1992.
- Skalsky, A., et al., Simultaneous plasma wave and electron flux observations upstream of the Martian bow shock, *Planet. Space Sci.*, *41*, 183, 1993.
- Skalsky A., et al., Wave observations at the foreshock boundary in the near Mars space, *Earth Planets and Space*, *50*, 439, 1998.
- Trotignon, J. G., R. Grard, and S. Klimov, Location of the Martian bow shock measurements by the plasma wave system on Phobos 2, *Geophys. Res. Lett.*, *18*, 365, 1991.
- Trotignon, J.-G., A. Skalsky, R. Grard, C. Nairn, and S. Klimov, Electron density in the Martian foreshock as a by-product of the electron plasma oscillation observations, *J. Geophys. Res.*, *97*, 10,831,840, 1992.
- Verigin, M. I., et al., On the problem of the Martian atmosphere dissipation: Phobos-2 TAUS spectrometer results, *J. Geophys. Res.*, *96*, 19,315, 1991.
- Zank, G. P., I. Pauls, H. Cairns, and M. Webb, Interstellar pickup ions and quasiperpendicular shocks: Implications for the termination shock and interplanetary shocks, *J. Geophys. Res.*, *101*, 457, 1996.
- Zhang, T. L., K. Schwingenschuh, and C. T. Russell, A study of the solar wind deceleration in the Earth's foreshock region, *Adv. Space Res.* *15* (8/9), 137, 1995.
- Zhang, T. L., K. Schwingenschuh, W. Riedler, G. Kotova, M. Verigin, M. Tatallyay, and C. T. Russell, Solar wind deceleration at Mars and Earth: A comparison, *Adv. Space Res.* *15*(2), 133, 1997.

---

M. Delva, and K. Schwingenschuh, Institut für Weltraumforschung, OAW, A-8010 Graz, Inffeldgasse 12, Austria. (delva@fiwf01.tu-gr.ac.at)

E. Dubinin, K. Sauer, and S. Livi Max-Planck Institut für Aeronomie, D-37191 Katlenburg-Lindau, Germany. (dubinin@linmpi.mpg.de)

R. Grard, Space Sciences Department, ESA/ESTEC, Postbus 299, 2200 AG, Noordwijk, The Netherlands. (rgrard@estec.esa.nl)

R. Lundin, Swedish Institute of Space Physics, Kiruna S-981, Sweden. (rickard@irf.se)

A. Skalsky, Space Research Institute, Profsoyuznaya 84/32, 117810 Moscow, Russia. (skalsky@mx.iki.rssi.ru)

K. Szego, KFKI Research Institute for Particle and Nuclear Physics, 29-33 Konkoly Thede str., Budapest, Hungary. (szego@rmki.kfki.hu)

J.-G. Trotignon, Laboratoire de Physiq. et de Chimie de l'Environnement/CNRS, 45071 Orleans Cedex 02, France. (jgtrotig@cns-orleans.fr)

(Received June 4, 1999; revised August 17, 1999; accepted August 24, 1999.)